

Turbulence Structure and Wall Signature in Hypersonic Boundary Layer

Yin-Chiu Kan*, Beekman Izaak†, M. Pino Martín‡

We demonstrate that a similar type of large-scale coherent structures, elongated and low-speed features, found in subsonic experiments, are present in our supersonic and hypersonic turbulent boundary layer datasets from direct numerical simulation (DNS). By estimating the conditional average of the velocity fields associated with spanwise swirling motions using linear stochastic estimation, hairpin structures are observed. Furthermore, correlations between wall wall signatures (e.g. wall-shear stress and wall-pressure fluctuations) and mass flux are performed and provide evidence of wall signatures associated with turbulence coherent structures. A two-dimensional finite impulse response (FIR) filter is applied on the instantaneous velocity field and wall signatures to show the relationship between the very long low-momentum region in the logarithmic layer and its associated wall signatures. In addition, an activity tracking algorithm that is developed based on feature-Petri net, a mathematical modeling language for the description of distributed systems, is employed to track individual packets and their wall signatures over space and time.

I. Introduction

Previous experimental and numerical studies have provided evidence of large-scale coherent vortical motions, or coherent structures, in turbulent wall-bounded flows. In 1952, Theodorsen¹ postulated the existence of hairpin vortex. He used a simple flow structure (shown in Figure 1(a)) to explain the formation of low-speed streamwise streaks and the ejection of near-wall low-momentum fluid into higher-momentum regions farther from the wall. In 1981, Head and Bandyopadhyay² found experimental evidence of individual hairpin vortices stacking and organizing into packets in the streamwise direction in turbulent boundary layers over a large range of Reynolds numbers ($500 < Re_\theta < 17500$), and they observed that the hairpin vortex heads form an envelope with a 15° to 20° downstream leaning angle with respect to the wall. In 2000, Adrian, Meinhart, and Tomkins³ proposed a hairpin packet model, where the hairpins align in the streamwise direction and organize into packets, as observed by Head and Bandyopadhyay. In this model, the low momentum regions are enclosed by hairpin packets. Therefore, hairpin heads and counter-rotating legs within the packets align in the streamwise direction and induce the low-momentum, very large-scale motions (VLSM) observed by Jiménez,⁴ Hutchins and Marusic⁵ and Kim and Adrian,⁶ see Figure 1(b). Moreover, Adrian *et al.*³ proposed that hairpin packets grow in size as they evolve and result in a nested packets that consist of hairpins or cane-type vortices growing up from the wall, with the older packets giving rise to younger and slower packets. Adrian *et al.*³ also found that hairpin vortices mostly appear as asymmetric cane-like vortices. Following this work, the term “hairpin” is used throughout to refer both to symmetric horseshoe-like vortices and asymmetric cane-like vortices.

Turbulence structures in boundary layers have been mostly studied in the subsonic flow regime (for example, Tomkins and Adrian;⁷ del Álamo and Jiménez;⁸ Ganapathisubramani, Longmire and Marusic;⁹ del Álamo *et al.*;¹⁰ del Álamo *et al.*;¹¹ Guala, Hommena and Adrian;¹² Hambleton, Hutchins and Marusic;¹³ Flores *et al.*;¹⁴ Balakumar and Adrian;¹⁵ Hutchins and Marusic⁵ and Mathis, Hutchins and Marusic¹⁶). In contrast, relatively few studies exist in the supersonic and hypersonic regimes due to the lack of detailed flow field data, and the studies have been mostly restricted to statistical analysis. For example, Smits *et*

*Graduate Student, Department of Aerospace Engineering, University of Maryland, College Park.

†Graduate Student, Department of Mechanical and Aerospace Engineering, Princeton University. Visiting Graduate Student, Department of Aerospace Engineering, University of Maryland, College Park.

‡AIAA Associate Fellow. Associate Professor, Department of Aerospace Engineering, University of Maryland, College Park.

al.,¹⁷ Spina, Donovan and Smits,¹⁸ and Smits and Dussauge¹⁹ were able to obtain the convection velocity, inclination angle, and length scale of the turbulent structure via space-time correlations. They found that structure properties change with both Mach and Reynolds number. More recently, advances in numerical techniques (Guarini *et al.*;²⁰ Martin;^{21,22} Pirozzoli, Grasso and Gatski;²³ Xu and Martin;²⁴ Ringuette, Wu and Martin²⁵ and experimental techniques (Elsinga *et al.*;²⁶ Schrijer, Scarano and van Oudheusden;²⁷ van Oudheusden;²⁸ Humble, Scarano and van Oudheusden²⁹) make possible for the acquisition of detailed four dimensional, in time and space, flow field data of supersonic/hypersonic turbulent boundary layers. In particular, both numerical^{25,30} and experimental^{26,31,32} data at supersonic Mach numbers have shown evidence of VLSM. For instance, Ganapathisubramani, Clemens and Dollings³¹ performed wide-field DPIV in a Mach 2 turbulent boundary layer and observed alternating streamwise structures of uniform low- and high-speed fluid in the logarithmic region with lengths exceeding their 8δ field of view. O’Farrell and Martin³³ were able to track the temporal evolution of hairpin packets and their wall signatures over a three-dimensional space and time Mach 3 DNS turbulent boundary layer data.

In this paper, we present statistical evidence for the existence of hairpin structures and their associated wall signatures in Mach 2.9 and Mach 7.2 spatially developing DNS turbulent boundary layer data. In Section II, we present the direct numerical simulation of Mach 2.9 ($Re_\tau \approx 650$) and Mach 7.2 ($Re_\tau \approx 550$) turbulent boundary layers over an adiabatic wall. In Section III and IV, we present the Mach number dependence of the size and the inclination angles of coherent structures at the logarithmic layer with various statistical methods. In addition, we examine the associated wall signatures of turbulent coherent structures via statistical tools and a spatial filtering technique. We demonstrate the usage of a finite impulse response spatial filter for visualizing the “superstructure” in the logarithmic layer and its associated wall signatures in the instantaneous flow field. In addition, we describe the activity tracking algorithm that is used to track evolution hairpin packets and their wall signatures.

II. DNS parameters and accuracy

To study the turbulent structures over boundary-layers, we use the spatially developing DNS dataset of a Mach 2.9 and a Mach 7.2 turbulent boundary layers over an adiabatic wall. The inflow boundary condition is provided by the rescaling technique outlined by Xu and Martin.²⁴ The boundary-layer edge conditions and wall parameters for both cases are given in Table 1, which provide boundary-layer edge Mach number, density and temperature, M_δ , ρ_δ and T_δ , respectively, and boundary-layer properties: momentum thickness (θ), shape factor $H = \delta^*/\theta$, where δ^* being the displacement thickness, Reynolds number based on momentum thickness, $Re_\tau = \rho_w u_\tau \delta / \mu_w$, and boundary-layer thickness δ . For both cases, the wall condition is adiabatic.

For the computational domain and grid resolution, the domain size, L/δ_0 where the value δ_0 is shown in table 2, and the number of grid points, N , for both cases are given in table 2, where the superscript (+) indicates scaling with inner or wall values. We take the streamwise, spanwise, and wall-normal directions to be x , y , and z , respectively. Grid resolutions in the streamwise, spanwise, and wall-normal direction are denoted in table 2 as Δx^+ , Δy^+ , and Δz^+ , respectively. The details of the numerical method are given by Xu and Martin,²⁴ and the accuracy of the simulations is validated in Beekman, Priebe, Kan, Martin,³⁴ and Priebe and Martin.³⁵ For the temporal tracking, the sampling rate is 1.20×10^{-6} sec and 1.02×10^{-6} sec for the Mach 2.9 case and the Mach 7.2 case, respectively, where structures travels approximately $0.1 \delta_0$ between each sample for both cases

Case	M_δ	ρ_δ (kg/m ³)	T_δ (K)	T_w/T_δ	Re_τ	Re_θ	θ (mm)	H	δ (mm)
Mach 2.9	2.91	0.0754	109.06	2.81	390–710	2620–4906	0.45–0.84	5.13	7.03–13.24
Mach 7.2	7.13	0.0765	64.31	10.10	373–575	11441–17682	0.60–0.92	24.23	24.21–37.48

Table 1. Freestream, boundary-layer, and wall parameters for the DNS.

Case	L_x/δ_0	L_y/δ_0	L_z/δ_0	δ_0 (mm)	N_x	N_y	N_z	Δ_x^+	Δ_y^+	Δ_z^+	Size
Mach 2.9	59.5	9.91	9.09	6.41	2520	1120	110	8.49	3.18	0.311	≈ 310 Million
Mach 7.2	54.0	9.00	19.7	20.4	2200	924	130	7.91	3.24	0.237	≈ 260 Million

Table 2. Grid resolution and domain size for the DNS. The grid is equispaced in the streamwise and spanwise directions and uses a geometric stretching in the wall normal direction. Here, $\Delta_z^+ = z_2 - z_1$

III. Structural Analysis

A. Linear Stochastic Estimation

To investigate the existence of hairpin structures at the present Reynolds and Mach numbers, a conditional average velocity field based on the presence of vortex core ($\langle u'(x', y', z') | E = \lambda_{ci,y} \cdot \text{sign}(\omega_y) > 0 \rangle$) would be suitable to examine the mean flow structure. The condition for the conditional average is chosen to be positive spanwise swirling strength motion ($\lambda_{ci,y} \cdot \text{sign}(\omega_y) > 0$) since hairpin vortex head is assumed to contain only positive spanwise swirling motions. However, it is computationally challenging to directly compute this conditional average. To simplify this impractical computation, linear stochastic estimation (LSE) could be used to estimate the conditional averages by minimizing the error between the conditional average and the estimate in mean-square sense.³⁶ It has been shown that the linear estimates are surprisingly accurate and simple to form for different types of turbulent flows.³⁶⁻³⁸ In short, the conditional average of the fluctuating velocity fields ($\langle u'(x', y', z') | E(x', y', z') \rangle$) is approximated by a linear function as Equation 1:

$$\langle u'(x', y', z') | E(x', y', z') \rangle \approx \frac{\langle u'(x' + \Delta x, y' + \Delta y, z) E(x', y', z') \rangle}{\langle E(x', y', z')^2 \rangle} E(x', y', z') \quad (1)$$

From Equation 1, it can be seen that the approximated conditional average is only a linear function of unconditional two-point correlation, which avoids the impractical computation of the conditional average. By assuming that the two-point correlations are independent in the streamwise and spanwise direction in boundary layer flow, Equation 1 becomes a function of Δx , Δy , and z . Since the DNS data is inhomogeneous in the streamwise direction, $\langle \dots \rangle$ denotes averaging over the spanwise direction, averaging over the streamwise direction with a specified window, and ensemble averaging over all snapshots. By employing linear stochastic estimation for the conditional average velocity fields associated to the presence of vortex core, Elsinga, Adrian, Van Oudheusden and Scarano³⁸ and Christensen and Adrian³⁷ successfully used the positive spanwise swirling strength ($\lambda_{ci,y} \cdot \text{sign}(\omega_y) > 0$) as the event vector to estimate the average conditional velocity fields and provided statistical evidence of hairpin structures in the subsonic channel flow and in the supersonic boundary layer flow.

By performing similar conditional averaging with LSE on the Mach 2.9 and Mach 7.2 datasets, the conditional eddies are found to be in hairpin shape in both cases (shown in Figure 2(a), 2(c), 3(a), and 3(c) in blue by swirling strength λ_{ci}), which reveal the the existence of hairpin vortices in the present Reynolds and Mach numbers. To obtain the estimated velocity associated to the hairpin head events, events with positive spanwise swirling strength ($\lambda_{ci,y} \cdot \text{sign}(\omega_y) > 0$) at $z = 0.35\delta_0$ are considered, which come out to be the same locations of hairpin heads shown in Figure 2(a), 2(c), 3(a), and 3(c). Both of the conditional eddies share similar shape and characteristics for Mach 2.9 and Mach 7.2. Consistent with previous studies by Elsinga *et al.*, the neck of both conditional eddies are approximately 45° downstream leaning with respect to the horizontal.³⁸ In terms of the eddy width, it is found to be approximately $0.15\delta_0$ in both datasets, which are 0.1δ shorter than what has been found in the previous study by Elsinga *et al.* with a relatively high Reynolds number supersonic boundary layer flow. At the event origin ($\Delta x = \Delta y = 0\delta_0, z = 0.35\delta_0$), the streamwise fluctuating velocity is found to be negative from the LSE, which implies that the eddies convect at a slower speed than the ensemble mean velocity; again, similar result has been found in Elsinga *et al.*³⁸ To examine the low momentum region underneath the eddies, iso-surface of $u' - u'_c$ is plotted. Both dataset share similar shape of the low momentum region, which extend from approximately $\Delta x = -1.125\delta_0$ to $\Delta x = 0.25\delta_0$ underneath the conditional eddies.

In Figure 2(b), 2(d), 3(b), and 3(d), vector fields of the fluctuating velocity are shown in a streamwise-wall-normal plane at $\Delta y = 0\delta_0$ and a streamwise-spanwise planes at $z = 0.2\delta_0$, respectively. To highlight the swirling motion at the event location ($\Delta x = \Delta y = 0\delta_0, z = 0.35\delta_0$), the streamwise velocity vector is

relative to the eddy convection velocity. As expected, strong counter-rotating swirling motions due to the hairpin legs are seen upstream of the event location in Figure 2(b) and 3(b); furthermore, strong positive spanwise swirling motions due to the hairpin neck are observed around the event location in Figure 2(d) and 3(d). More importantly, a shear layer upstream of the hairpin and an ejection event ($u' < 0, w' > 0$) due to the hairpin legs can be seen, as expected.

B. Autocorrelations of Mass Flux

Duan, Beekman and Martin³⁹ performed autocorrelation of mass flux on the DNS datasets with various Mach numbers under approximately the same Reynolds number to investigate the Mach number dependence of the size and inclination angle for typical eddies in the logarithmic layer ($z = 0.2\delta_0$). They observed similar size in and inclination angle in Mach 0.3 and Mach 2.9 dataset. Furthermore, they found that the size of eddies in the streamwise direction decreased and structures inclination angle increased as Mach number increased from 2.9 to 11.9.

By performing the similar analysis on the Mach 2.9 and Mach 7.2 datasets, Figure 4(a) and 4(b) show the contour maps on streamwise-wall-normal planes and streamwise-spanwise planes for the autocorrelations of mass flux with origin at $z=0.2\delta_0$, respectively. Consistent with the observation by Duan *et al.*,³⁹ the streamwise length of the structure detected by the mass flux autocorrelations in the Mach 2.9 case is larger than in the Mach 7.2 case, whereas the inclination angle of the structure in the Mach 2.9 case is smaller than in the Mach 7.2 case. The inclination angle of the structure is approximately 14° for the Mach 2.9 case, whereas the inclination angle increases to approximately 25° in the Mach 7.2 case. Note that negative correlation coefficients are found in the streamwise-spanwise plane for both cases, this is an indication of the sweep events outside the hairpin legs ($(\rho u)' > 0$ outside the legs and $(\rho u)' < 0$ at the origin).

IV. Wall Signatures of Coherent Structures

A. Brown and Thomas Correlation

Brown and Thomas⁴⁰ were able to use the correlations between the wall shear stress and streamwise velocity at a single reference location over different wall-normal distances to detect large-scale structures in the boundary layer. From the correlation profile, the correlation peak were found to be at an increasing downstream distance with increasing wall-normal location, which indicated the presence of downstream-leaning coherent structure. In addition, Ringuette, Wu and Martin,²⁵ Duan *et al.*,³⁹ O'Farrell and Martin,³³ and Marusic and Heuer⁴¹ applied the similar method on the boundary layer flow to examine the wall signatures of the coherent structures and successfully detected the structures inclination angles. By following the analysis by Duan *et al.*,³⁹ correlations between the wall-shear stress and streamwise mass flux, defined by Equation 2, is performed on both the Mach 2.9 and Mach 7.2 cases.

$$R_{\tau'_w(\rho u)'} = \frac{\langle \tau'_w(x, y)(\rho u)'(x + \Delta x, y + \Delta y, z) \rangle}{\langle \tau'_{w,rms}(\rho u)'_{rms} \rangle} \quad (2)$$

Figure 5(a) and 5(b) plot the contour maps of $R_{\tau'_w(\rho u)'}$ in the streamwise-wall-normal and streamwise-spanwise planes at $z = 0.2\delta_0$ for both cases, respectively. As expected, downstream leaning structures are detected in both cases. By comparing the inclination angles with the contour maps of $R_{(\rho u)'(\rho u)'}$, the structure inclination angles, detected by the Brown and Thomas correlations, are shallower for both cases. This is likely due to the wall-shear stress signatures caused by the coherent structures being more localized near the wall. To understand the contour maps shown in Figure 5(a) and 5(b), $R_{\tau'_w(\rho u)'}$ can be thought as a measure of how the wall-shear stresses react to the organized structures, and it can be seen that the contour maps follow the hairpin packet model by Adrian *et al.*³ According to the model, a low momentum region is induced in the core of the hairpin packet by the surrounding vortices. In the contour maps, positive $R_{\tau'_w(\rho u)'}$ reflects the appearance of ejection events, where low momentum fluids with negative $(\rho u)'$ reduce the drag or wall-shear stresses at the wall (negative τ'_w); thus, $R_{\tau'_w(\rho u)'}$ becomes positive. Similarly, fluids gain momentum from the sweep events outside the hairpin legs that cause positive $(\rho u)'$, and correlate with the negative τ'_w at the origin, which result in negative $R_{\tau'_w(\rho u)'}$. Thus, the inclination angle in the contour maps is indication of the hairpin packets. By comparing Figure 5(a) and 5(b), it can be seen that they share similar shape; in consistent with the results of mass flux autocorrelation, the streamwise length of the structure is shorter for Mach 7.2 case. In Figure 6(a) and 6(b), three dimensional distributions of $R_{\tau'_w(\rho u)'}$

are plotted for both Mach 2.9 and Mach 7.2 to better visualize the hairpin packets detected by the Brown and Thomas correlations. Similar to the two dimensional contour plots shown in Figure 5(a) and 5(b), positive regions, correspond to the ejection events, sit in between negative regions that correspond to the sweep events, which is further evidence of the existence and importance of hairpin packets conceptualized by Adrian *et al.*³

B. Correlaton between wall pressure and mass flux

To further investigate the wall signatures of turbulence coherent structures, correlations between wall pressure and mass flux are performed on both datasets. The correlation coefficient is defined as Equation 3.

$$R_{p'_w(\rho u)'} = \frac{\langle p'_w(x, y)(\rho u)'(x + \Delta x, y + \Delta y, z) \rangle}{\langle p'_{w,rms}(\rho u)'_{rms} \rangle} \quad (3)$$

Figure 7(a) and 7(b) plot the contour maps of $R_{p'_w(\rho u)'}$ in the streamwise wall-normal and streamwise spanwise planes at $z = 0.2\delta_0$ for both cases. Similar to the result from Brown and Thomas correlations, downstream leaning structures are detected for both cases. In contrast to the result of Brown and Thomas correlations, the wall-pressure correlation is able to detect the motions in the outer layer unlike the wall-shear stress. As mentioned in Section IVA, the wall-shear stress is a relatively localize quantity near wall as it is governed by the streamwise velocity gradient at the wall, whereas the wall-pressure is a quantity that could be induced by more distant vortical motions; therefore, it could more sensitive to the motions away from the wall. Interestingly, two downstream leaning structures are detected in each dataset as shown in Figure 7(a) and 7(b). A structure with positive correlation coefficients can be seen upstream of the origin followed by a structure with negative correlation coefficients downstream of the origin. In both datasets, it can be observed that the inclination angles of the structures upstream are steeper than the the structures downstream. Furthermore, the structures upstream are surrounded by two bands of zero contour lines, which represent zero fluctuating velocity, which are found to be consistent with a previous study by Snarski and Lueptow,⁴² who performed a measurement of wall-pressure and streamwise velocity fluctuations in an incompressible turbulent boundary layer. In their study, they hypothesized a conceptual model of large-scale boundary layer structures, shown in Figure 8, to interpret the contour maps. In the conceptual model, they assumed that a secondary vortex with opposite rotation is induced by the shear created between the adjacent faces of two large-scale vortices. As shown in Figure 8, the streamwise velocity fluctuations are zero along the bisectors of the counter-rotating vortices and large-scale vortices (shown as bold dashed lines). Therefore, two bands of zero contour lines appear in the contour maps. For the structures with positive correlation, they assumed that positive correlation is due to high speed fluid ($(\rho u)' > 0$), which causes a positive $R_{p'_w(\rho u)'}$ when correlating with a positive p'_w . By assuming that the streamwise velocity fluctuations are the largest at the top of the large-scale vortical structures, the upstream structure with positive correlation in the contour maps could be thought as the leading face of the large-scale vortices; thus, it has a steeper inclination angle. By using similar argument, the negative $R_{p'_w(\rho u)'}$ is the cause by the low speed fluid ($(\rho u)' < 0$) correlating with positive p'_w . Again, by assuming that the streamwise velocity fluctuations are the largest in magnitude with a negative sign at the bottom of the vortical structures. This forms the downstream structures with negative correlation in the contour maps, and offers an explanation for the shallower inclination angle. In Figure 9(a) and 9(b), three dimensional distributions of $R_{p'_w(\rho u)'}$ are plotted for both Mach 2.9 and Mach 7.2 to better visualize the structures captured by the correlation between wall-pressure and mass flux. Similar to the three dimensional distributions of $R_{\tau'_w(\rho u)'}$, a region with long streamwise length regions in the middle are surrounded by negative regions. In the middle, a positive region with a steeper inclination angle upstream to the origin is followed by a negative region with a slight shallower inclination angle, as seen in the two dimensional contour maps. In terms of the negative regions, it could be seen that they have similar shapes to the negative regions observed from the plots of the three dimensional Brown and Thomas correlation coefficients shown in Figure 6(a) and 6(b). Thus, sweep events with $p'_w < 0$ and $(\rho u)' > 0$ outside the hairpin legs could be a potential explanation for it.

V. Instantaneous Flow Field

Brown and Thomas,⁴⁰ and Thomas and Bull⁴³ performed experiments with incompressible turbulent boundary layers and showed characteristic patterns in the wall-shear stress and wall-pressure, which are

hypothesized to be associated with large-scale coherent motions. Figure 10 is a reproduction of a schematic from the paper by Thomas and Bull,⁴³ which shows a large-scale, coherent motion together with the associated wall shear stress and pressure signatures. Furthermore, Section IV provides evidences to support the hypothesis by Thomas and Bull.⁴³ Here, we would like to examine the associated wall-signatures of coherent motions in the instantaneous fields. Figure 12 and 14 plot the normalized streamwise mass flux fluctuation, normalized wall-shear stress fluctuation, and normalized wall-pressure fluctuation in the instantaneous field for the Mach 2.9 and Mach 7.2, respectively. To examine the associated wall signatures and coherent motions, we used a two dimensional finite impulse response (FIR) filter with a anisotropic, bi-variate Gaussian distribution of zero cross correlation to remove fluctuations which are smaller than hairpin packets based on the Brown and Thomas⁴⁰ correlation contour maps computed in Section IVA. As an example, a sample filter, captured from Beekman *et al.*,³⁴ with $2.5\delta_0$ streamwise filtering halfwidth and $0.65\delta_0$ spanwise filtering halfwidth is shown in Figure 11. In Beekman, Priebe, Kan and Martin,³⁴ they were able to show the existence of “superstructures” in the logarithmic layer by applying the filter shown in Figure 11 on the streamwise mass flux fluctuations at $z=0.2\delta_0$. More importantly, they were able to show an almost one to one correspondence between the wall-shear stress signatures and the “superstructures” at the logarithmic layer.

By performing the same analysis with the appropriate filtering halfwidth based on the Brown and Thomas correlations coefficient contour maps in Figure 5(a) and 5(b), a low-pass normalized streamwise mass flux fluctuation and normalized wall-shear stress fluctuation are obtained for both Mach 2.9 and Mach 7.2 as shown in Figure 13(a-b) and 15(a-b). As expected, almost one to one correspondence between the wall-shear stress signatures and the low momentum streaks are observed in both datasets. In addition to the wall-shear stress signature, wall-pressure signatures are examined similarly. Here, we define the filter halfwidth according to the contour maps of the wall-pressure mass flux correlation computed in Section IVB. Figure 13(c) and 15(c) plot the low-pass wall-pressure field. By comparing to the low-pass streamwise mass flux fluctuation field, the wall-pressure signatures associated with the “superstructures” could barely be seen. As mentioned in Section IVB, the wall-pressure is very sensitive to any kind of vortical motions inside or even outside the boundary layer edge as shown in the correlation between the wall-pressure and mass flux. Therefore, the instantaneous wall-pressure could be noisy due to the vortical motions from different scales, which makes it challenging to examine the wall-pressure signatures due to the “superstructures”.

VI. Activity Tracking Algorithm

O’Farrell and Martin³³ used the Object Segmentation and Feature Tracking (Ostrk2.0) software package^{44,45} to identify individual hairpin packets and track their evolution through consecutive flow realizations on DNS data of a Mach 3 turbulent boundary layer. The tracking software performs tasks in three levels, which are Feature Tracking, Grouping, and Group Tracking, on the instantaneous swirling strength fields. To summarize, the tracking software extracts and tracks hairpin or cane-like vortices, based on the user-specified threshold ($4.5\lambda_{ci}^2$) at Feature Tracking level and groups hairpin vortices into ideal packets that conform with the criteria of Ringuette, Wu and Martin,²⁵ at the Grouping level. Finally, the group tracking level is used to temporally track the evolution of packets. Further details on Ostrk2.0 could be found in the User Manual by Liang,⁴⁴ and the paper by Wang and Silver.⁴⁵ O’Farrell and Martin³³ find that the software mistakenly merge the neighboring vortices into a packets showing unphysical proliferation of packets. Thus, they were not able to obtain satisfactory results from Ostrk2.0.

Recently, Sedat, Silver, Bemis, Martin, and Takle⁴⁶ implement one more level, called higher level grouping (see Figure 16(a)), onto Ostrk2.0 which performs cross-level interactions of the group tracking level to improve the accuracy of the temporal tracking evolution of packets without unphysical growth. By applying the improved activity tracking algorithm to our Mach 2.9 data, Figure 17 shows an iso-surface of the swirling strength equal to $4.5\lambda_{ci}^2$ of a geometrically strong packet in four time realizations.

By using the activity tracking algorithm, we have tracked two hairpin packets, highlighted in solid colors in Figure 18 and Figure 21, for each Mach 2.9 and Mach 7.2. After tracking this packet and watching its evolution, we monitored their wall signatures at two time instances. Figure 19(c-d) and Figure 20(c-d) show the wall-pressure and the wall-shear stress of the associated packets at a selected time instance and at a time instance where the packets traveled a distance of approximately δ_0 . In both figures, visualizations of the identified packets in streamwise-wall normal plane and streamwise-spanwise plane are plotted with iso-surfaces of the swirling strength at $4.5\lambda_{ci}^2$. In addition, Figure 22 and Figure 23 plot the same content for

the Mach 7.2 case. For all cases shown in Figure 19, 20, 22, and 23, hairpin vortices within the identified packets are cane-like with sets of asymmetric counter rotating legs. Consistent with the hypothesis by Brown and Thomas⁴⁰ and Thomas and Bull,⁴³ a significant peak could be observed in both the wall-shear stress and wall-pressure signals associated with the hairpin legs.

VII. Conclusions

Through the linear stochastic estimation of the conditional averages, hairpin vortices structures are found to be existed in both Mach 2.9 and Mach 7.2 boundary layers. By performing the streamwise mass flux autocorrelations, Brown and Thomas correlations, and wall-pressure streamwise mass flux fluctuations correlation in Section III B and IV, downstream leaning structures are found. Consistent with Duan *et al.*,³⁹ it has been found that the inclination angle of the coherent structure increases as Mach number increases, whereas the streamwise length of the coherent structures decreases as Mach number increases. Furthermore, wall signatures associated with the coherent structures are examined with statistical methods. The results of the Brown and Thomas correlations provide evidence to support the hairpin packet model by Adrian *et al.*³ Also, the result from the wall-pressure streamwise mass flux fluctuations correlation provides evidence for the wall signatures associated with large-scale coherent structure hypothesis by Thomas and Bull⁴³ and Snarski and Lueptow⁴² as discussed in Section IV. To examine the wall signature in the instantaneous field, wall-shear stress signatures are found to be highly associated with the “superstructures”, as seen from the low-pass filtered field. To further investigate the wall signatures of hairpin packets, we use the activity tracking algorithm by Sedat, Silveris, Bemis, Martin, and Takle⁴⁶ (discuss in Section VI) to track the temporal evolutions of packets and their wall signatures. By observing the evolutions, characteristic patterns of wall signatures associated with the hairpin legs, hypothesized by Brown and Thomas⁴⁰ and Thomas and Bull,⁴³ are observed in the supersonic and hypersonic turbulent boundary layer DNS datasets.

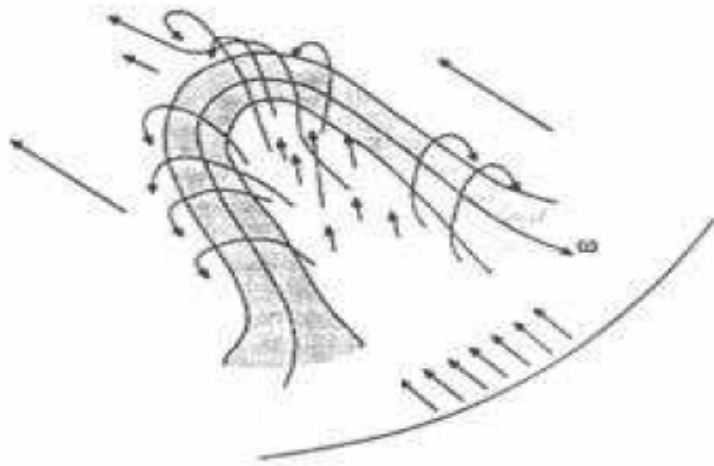
Acknowledgments

This work is supported by the Air Force Office of Scientific Research under grant AF/9550-10-1-0535 “STW 21 - Revitalization of the Hypersonics Testing and Evaluation Workforce.”

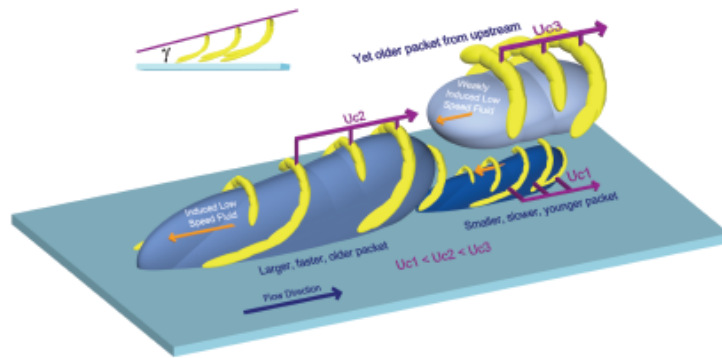
References

- ¹Theodorsen, T., “Mechanism of Turbulence,” *Proc. 2nd. Midwestern Conf. on Fluid Mech.*, Ohio State University, Columbus, Ohio, USA, 1952, pp. 1–19.
- ²Head, M. and Bandyopadhyay, P., “New aspects of turbulent boundary-layer structure,” *J. Fluid Mech.*, Vol. 107, 1981, pp. 297–338.
- ³Adrian, R., Meinhart, C., and Tomkins, C., “Vortex organization in the outer region of the turbulent boundary layer,” *J. Fluid Mech.*, Vol. 422, 2000, pp. 1–54.
- ⁴Jiménez, J., “The largest scales of turbulent wall flows,” *Center for Turbulence Research, Annual Research Briefs*, Stanford University, 1998, pp. 137–154.
- ⁵Hutchins, N. and Marusic, I., “Evidence of very long meandering features in the logarithmic region of turbulent boundary layers,” *J. of Fluid Mechanics*, Vol. 579, 2007, pp. 1–28.
- ⁶Kim, K. C. and Adrian, R. J., “Very large-scale motion in the outer layer,” *Phys. Fluids*, Vol. 11, No. 2, 1999, pp. 417–422.
- ⁷Tomkins, C. and Adrian, R., “Spanwise structure and scale growth in turbulent boundary layers,” *J. Fluid Mech.*, Vol. 490, 2003, pp. 37–74.
- ⁸del Álamo, J. C. and Jiménez, J., “Spectra of the very large anisotropic scales in turbulent channels,” *Phys. Fluids*, Vol. 15, No. 6, 2003, pp. L41–L44.
- ⁹Ganapathisubramani, B., Longmire, E. K., and Marusic, I., “Characteristics of vortex packets in turbulent boundary layers,” *J. Fluid Mech.*, Vol. 478, 2003, pp. 35–46.
- ¹⁰del Álamo, J. C., Jiménez, J., Zandonade, P., and Moser, R. D., “Scaling of the energy spectra of turbulent channels,” *J. Fluid Mech.*, Vol. 500, 2004, pp. 135–144.
- ¹¹del Álamo, J. C., Jiménez, J., Zandonade, P., and Moser, R. D., “Self-similar vortex clusters in the turbulent logarithmic region,” *J. Fluid Mech.*, Vol. 561, 2006, pp. 329–358.
- ¹²Guala, M., Hommema, S. E., and Adrian, R. J., “Large-scale and very-large-scale motions in turbulent pipe flow,” *J. Fluid Mech.*, Vol. 554, 2006, pp. 521–542.
- ¹³Hambleton, W. T., Hutchins, N., and Marusic, I., “Simultaneous orthogonal-plane particle image velocimetry measurements in a turbulent boundary layer,” *J. Fluid Mech.*, Vol. 560, 2006, pp. 53–64.
- ¹⁴Flores, O., Jiménez, J., and del Álamo, J. C., “Vorticity organization in the outer layer of turbulent channels with disturbed walls,” *J. Fluid Mech.*, Vol. 591, 2007, pp. 145–154.

- ¹⁵Balakumar, B. J. and Adrian, R. J., "Large- and very-large-scale motions in channel and boundary-layer flows," *Phil. Trans. R. Soc. A*, Vol. 365, 2007, pp. 665–681.
- ¹⁶Mathis, R., Hutchins, N., and Marusic, I., "Large-scale amplitude modulation of the small-scale structures in turbulent boundary layers," *J. Fluid Mech.*, Vol. 628, 2009, pp. 311–337.
- ¹⁷Smits, A., Spina, E., Alving, A., Smith, R., Fernando, E., and Donovan, J., "A comparison of the turbulence structure of subsonic and supersonic boundary layers," *Phys. Fluids A*, Vol. 1, 1989, pp. 1865–1875.
- ¹⁸Spina, E., Donovan, J., and Smits, A., "On the structure of high-Reynolds number supersonic turbulent boundary layers," *J. Fluid Mech.*, Vol. 222, 1991, pp. 293–327.
- ¹⁹Smits, A. J. and Dussauge, J.-P., *Turbulent shear layers in supersonic flow*, Springer, 2nd ed., 2006.
- ²⁰Guarini, S., Moser, R., Shariff, K., and Wray, A., "Direct numerical simulation of supersonic turbulent boundary layer at Mach 2.5," *J. of Fluid Mech.*, Vol. 414, 2000, pp. 1–33.
- ²¹Martín, M. P., "DNS of hypersonic turbulent boundary layers," *AIAA Paper 2004-2337*, 2004.
- ²²Martín, M. P., "Direct numerical simulation of hypersonic turbulent boundary layers. Part 1: Initialization and comparison with experiments," *J. Fluid Mech.*, Vol. 570, 2007, pp. 347–364.
- ²³Pirozzoli, S., Grasso, F., and Gatski, T., "Direct numerical simulation and analysis of a spatially evolving supersonic turbulent boundary layer at $M=2.25$," *Phys. Fluids*, Vol. 16, No. 3, 2004, pp. 530 – 545.
- ²⁴Xu, S. and Martín, M., "Assessment of Inflow Boundary Conditions for Compressible Turbulent Boundary Layers," *Physics of Fluids*, Vol. 16, No. 7, 2004, pp. 2623–2639.
- ²⁵Ringuette, M. J., Wu, M., and Martín, M. P., "Coherent structures in direct numerical simulation of turbulent boundary layers at Mach 3," *J. Fluid Mech.*, Vol. 594, 2008, pp. 59–69.
- ²⁶Elsinga, G., Adrian, R., Van Oudheusden, B., and Scarano, F., "Three-dimensional vortex organization in a high-Reynolds-number supersonic turbulent boundary layer," *J. of Fluid Mech.*, Vol. 644, 2010, pp. 35–60.
- ²⁷Schrijer, F., Scarano, F., and van Oudheusden, B., "Application of PIV in a Mach 7 double-ramp flow," *Experiments in Fluids*, Vol. 41, 2006, pp. 353–363.
- ²⁸van Oudheusden, B., "Principles and application of velocimetry-based planar pressure imaging in compressible flows with shocks," *Experiments in Fluids (electronic Open Access)*, 2008.
- ²⁹Humble, R., Scarano, F., and van Oudheusden, B., "Experimental study of an incident shock wave/turbulent boundary layer interaction using PIV," *AIAA Paper Number*, Vol. number 2006-3361, 2006.
- ³⁰Wu, M. and Martín, M., "Direct numerical simulation of shockwave and turbulent boundary layer interactions over a compression ramp," *AIAA J.*, Vol. 45, 2007, pp. 879–889.
- ³¹Ganapathisubramani, B., Clemens, N., and Dolling, D., "Large-scale motions in a supersonic turbulent boundary layer," *J. Fluid Mech.*, Vol. 556, 2006, pp. 1–11.
- ³²Ganapathisubramani, B., Clemens, N., and Dolling, D., "Effects of upstream boundary layer on the unsteadiness of shock-induced separation," *J. Fluid Mech.*, Vol. 585, 2007, pp. 369–394.
- ³³O'Farrel, C. and Martin, M. P., "Chasing Eddies and Their Wall Signature in DNS Data of Turbulent Boundary Layers," *J. Turbulence*, N15, 2010.
- ³⁴Beekman, I., Priebe, S., Kan, Y., and Martin, M. P., "DNS of a Large-Domain, Mach 3 Turbulent Boundary Layer: Turbulence Structure," *AIAA Paper No. 2011-753*, Jan 2011.
- ³⁵Priebe, S. and Martin, M. P., "Low-frequency Unsteadiness in Shock Wave-turbulent Boundary Layer Interaction," 2012, pp. 1–49.
- ³⁶Adrian, R. J., "Linking Correlations and Structure: Stochastic estimation and conditional averaging," *Zoran P. Zaric Memorial International Seminar on Near-Wall Turbulence*.
- ³⁷Christensen, K. T. and Adrian, R. J., "Statistical Evidence of Hairpin Vortex Packets in Wall Turbulence," *J. Fluid Mech.*, Vol. 431, 2001, pp. 433–443.
- ³⁸Elsinga, G. E., Adrian, R. J., Van Oudheusden, B. W., and Scarano, F., "Three-dimensional vortex organization in a high Reynolds number supersonic turbulent boundary layer," *J. Fluid Mech.*, Vol. 664, 2010, pp. 35–60.
- ³⁹Duan, L., Beekman, I., and Martin, M. P., "Direct numerical simulation of hypersonic turbulent boundary layers. Part 3. Effect of Mach number," *J. Fluid Mech.*, Vol. 672, 2010, pp. 245–267.
- ⁴⁰Brown, G. L. and Thomas, A. S. W., "Large structure in a turbulent boundary layer," *Phys. Fluids*, Vol. 10, No. 2, 1977, pp. 243–251.
- ⁴¹Marusic, I. and Heuer, W. D., "Reynolds number invariance of the structure inclination angle in wall turbulence," *Physical Review Letters*, Vol. 99, 2007, pp. 1–4.
- ⁴²Snarski, S. R. and Lueptow, R. M., "Wall pressure and coherent structures in a turbulent boundary layer on a cylinder in axial flow," *J. Fluid Mech.*, Vol. 286, 1995, pp. 137–171.
- ⁴³Thomas, A. S. W. and Bull, M. K., "On the role of wall-pressure fluctuations in deterministic motions in the turbulent boundary layer," *J. Fluid Mech.*, Vol. 128, 1983, pp. 283–322.
- ⁴⁴Liang, L., "User Manual for Object-Segmentation and Feature-Tracking (ostrk2.0) Using AVS/exp Package," Tech. rep., Rutgers, The State University of New Jersey, 2003.
- ⁴⁵Wang, X. and Silver, D., "Tracking and Visualizing Turbulent 3D Features," *IEEE Transactions on Visualization and Computer Graphics*, Vol. 3, No. 2, 1997, pp. 129–141.
- ⁴⁶Ozer, S., Silver, D., Bemis, K., Martin, M. P., and Takle, J., "Activity Detection for Scientific Visualization," *Large Data Analysis and Visualization (LDAV), 2011 IEEE Symposium*, 2011, pp. 117–118.



(a) Theodorsen's hairpin vortex.¹ The arrows on either side of the hairpin indicate the direction of the flow.



(b) Very large scale motion model of Adrian *et al.*³ in which hairpin packets align to produce the long, low-momentum streaks in the logarithmic layer.

Figure 1. Coherent boundary layer structures. Figures from Theodorsen¹ and Adrian *et al.*³

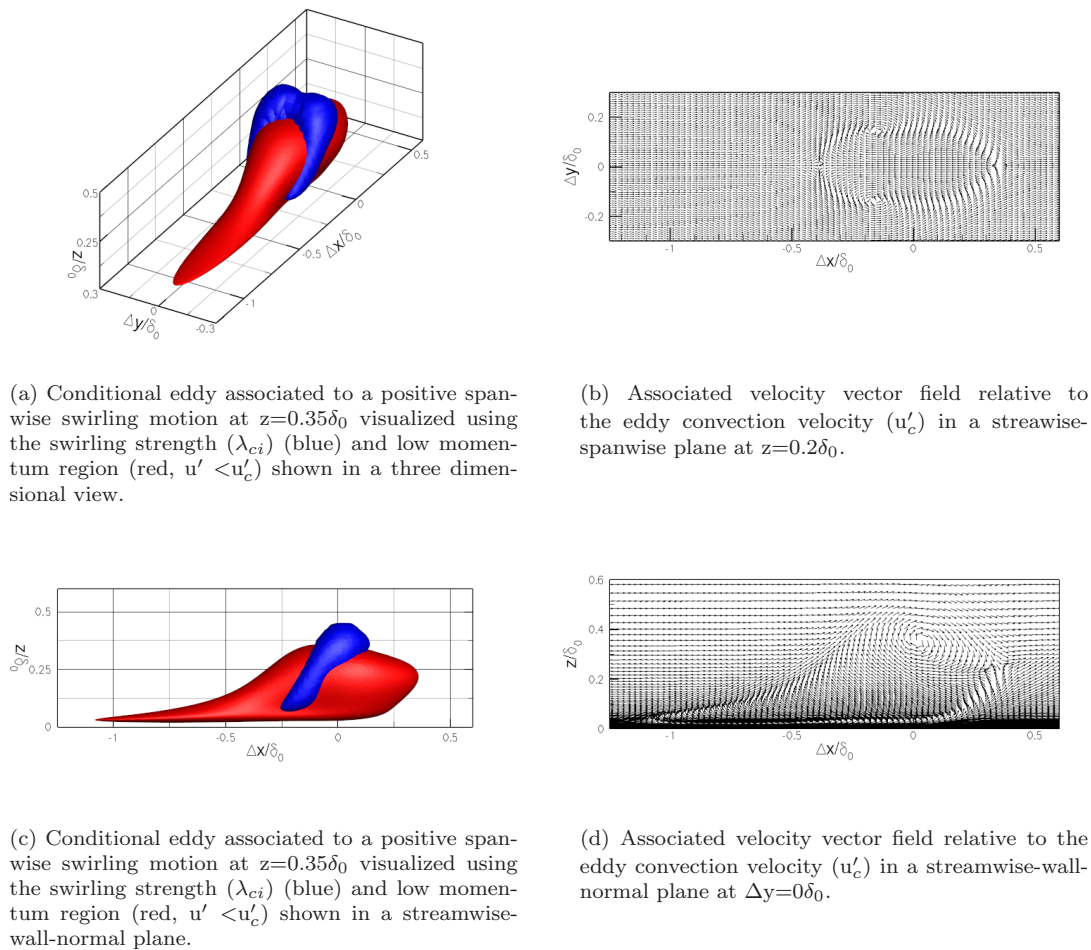


Figure 2. The estimated conditional eddy and its corresponding velocity vector field associated to a positive spanwise swirling motion at $z=0.35\delta_0$ for the Mach 2.9.

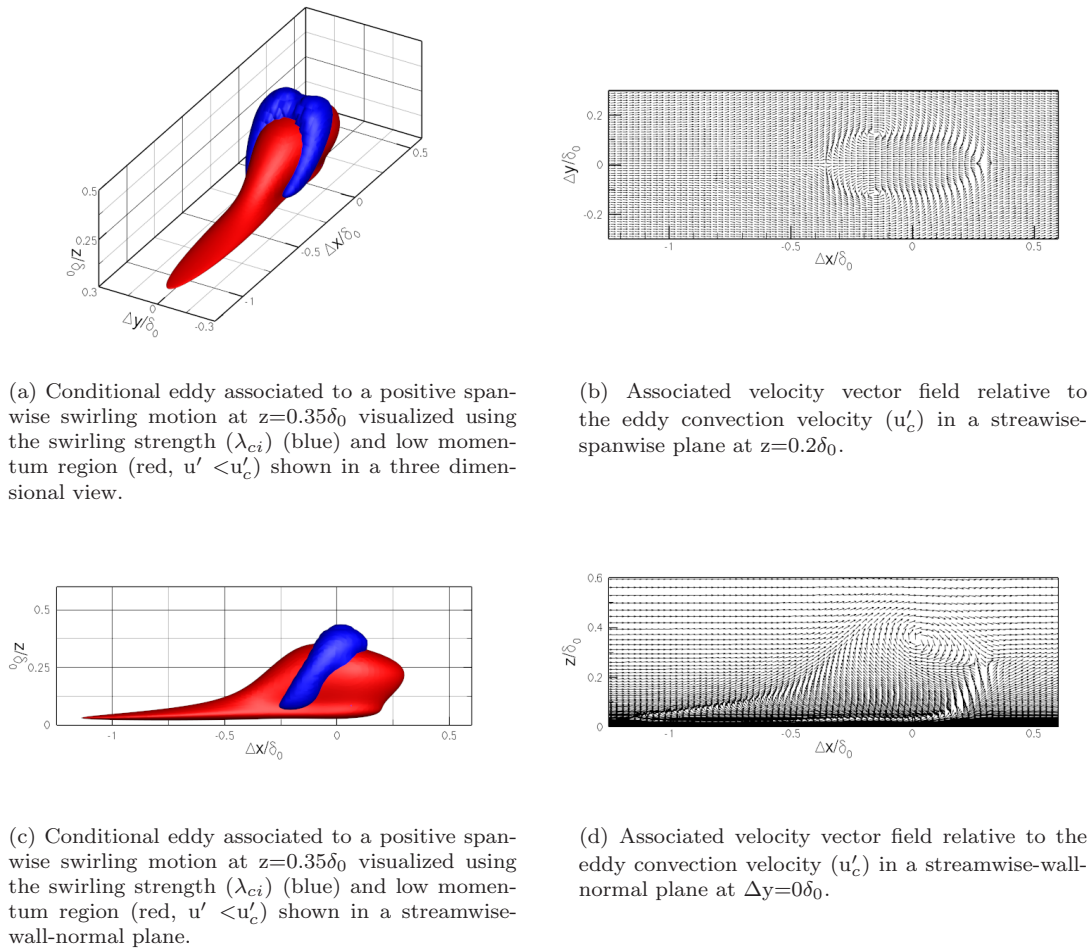
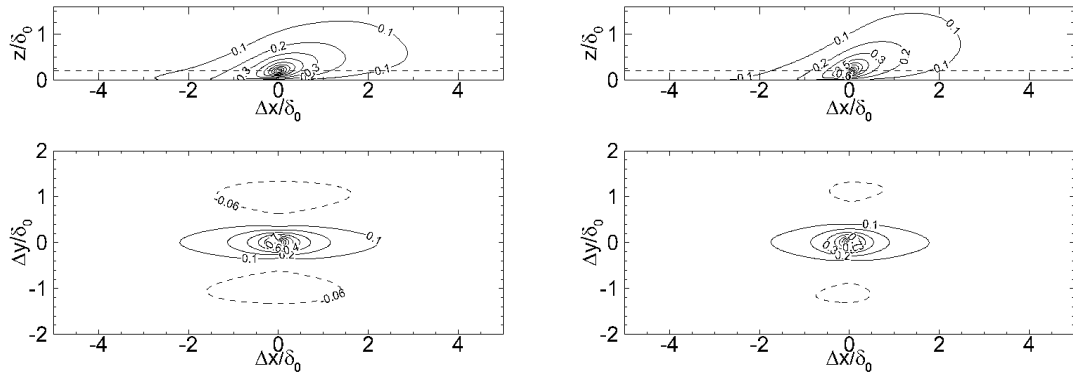


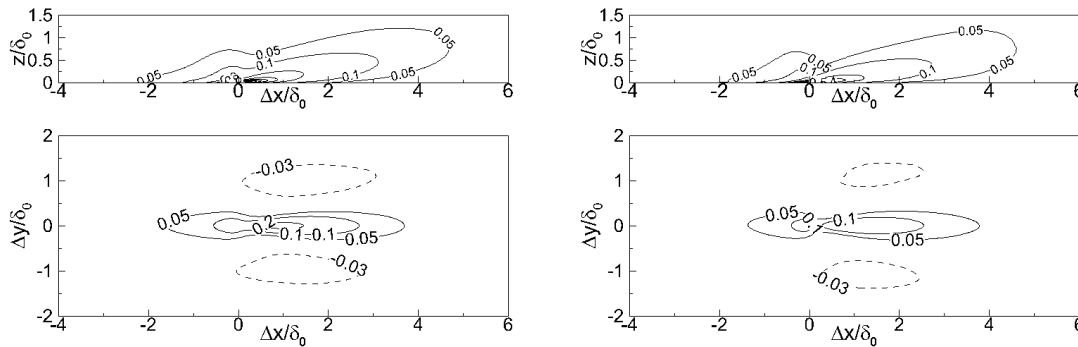
Figure 3. The estimated conditional eddy and its corresponding velocity vector field associated to a positive spanwise swirling motion at $z=0.35\delta_0$ for the Mach 7.2.



(a) Autocorrelation contour maps of $R_{(\rho u)'(\rho u)'}$ on a streamwise-wall-normal plane (top) and streamwise-spanwise plane at $z=0.2\delta_0$ (bottom) for Mach 2.9.

(b) Autocorrelation contour maps of $R_{(\rho u)'(\rho u)'}$ on a streamwise-wall-normal plane (top) and streamwise-spanwise plane at $z=0.2\delta_0$ (bottom) for Mach 7.2.

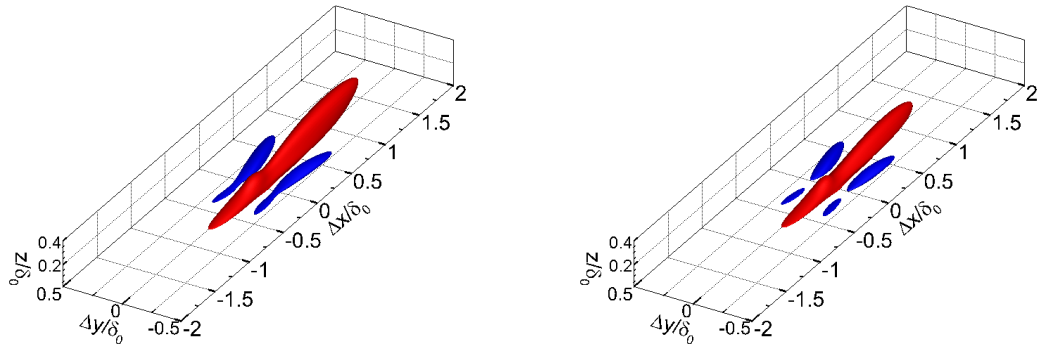
Figure 4. Autocorrelation contour maps of mass flux fluctuation with fixed origin at $z=0.2\delta_0$.



(a) Contour maps of $R_{\tau_w'(\rho u)'}$ on a streamwise-wall-normal plane (top) and streamwise-spanwise plane at $z=0.2\delta_0$ (bottom) for Mach 2.9.

(b) Contour maps of $R_{\tau_w'(\rho u)'}$ on a streamwise-wall-normal plane (top) and streamwise-spanwise plane at $z=0.2\delta_0$ (bottom) for Mach 7.2.

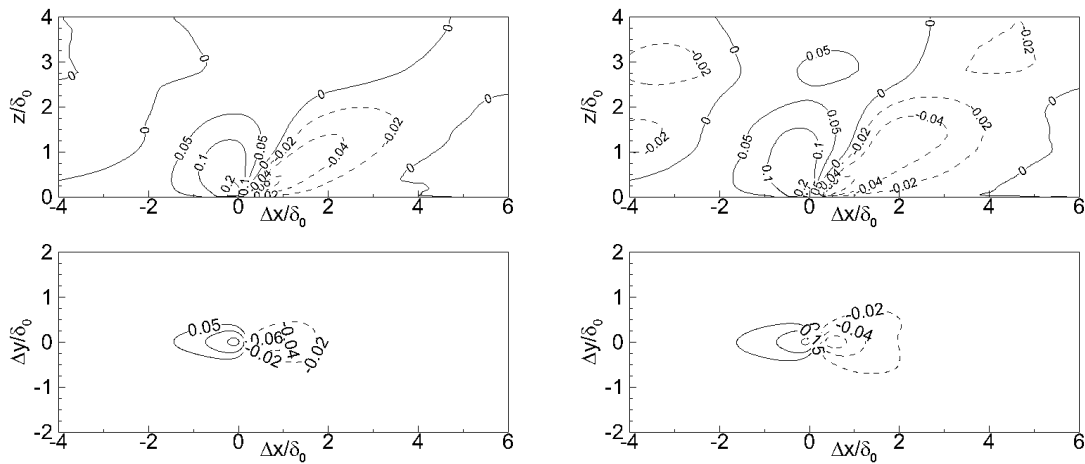
Figure 5. Brown and Thomas correlation contour maps.



(a) Iso-surface of $R_{\tau_w'(\rho u)'}$ to visualize vortical structure for Mach 2.9. Iso-surface value of the correlation coefficient at 0.2 shown in red and at -0.02 in blue.

(b) Iso-surface of $R_{\tau_w'(\rho u)'}$ to visualize vortical structure for Mach 7.2. Iso-surface value of the correlation coefficient at 0.2 shown in red and at -0.02 in blue.

Figure 6. Three dimensional distribution of Brown and Thomas correlation coefficient.



(a) Contour maps of $R_{p_w'(\rho u)'}$ on a streamwise-wall-normal plane (top) and streamwise-spanwise plane at $z=0.2\delta_0$ (bottom) for Mach 2.9.

(b) Contour maps of $R_{p_w'(\rho u)'}$ on a streamwise-wall-normal plane (top) and streamwise-spanwise plane at $z=0.2\delta_0$ (bottom) for Mach 7.2.

Figure 7. Correlation contour maps between wall-pressure and mass flux fluctuations.

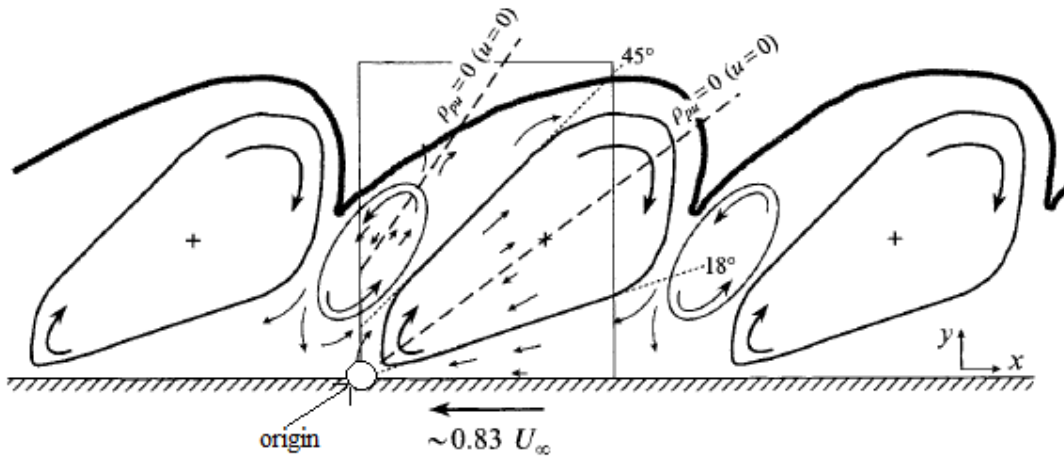
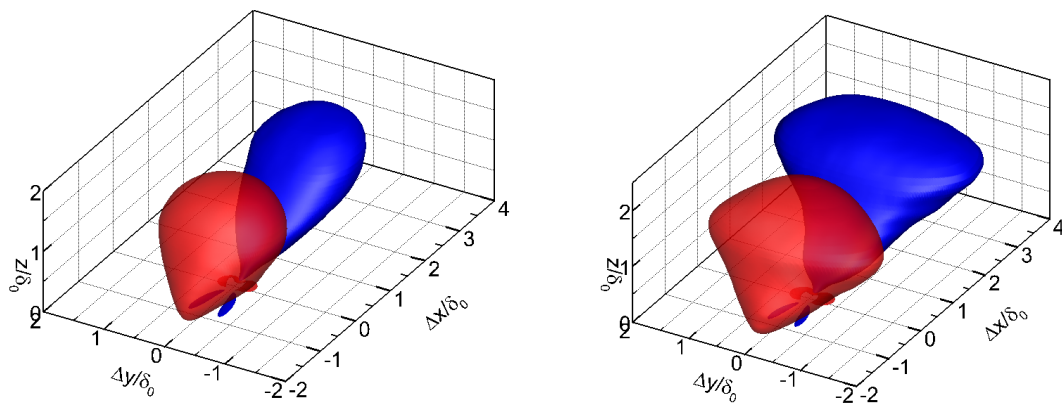


Figure 8. Conceptual model of large-scale boundary layer structure by Snarski and Lueptow,⁴² Figure from Snarski and Lueptow⁴²



(a) Iso-surface of $R_{p'_w(\rho u)'}$ to visualize vortical structure for Mach 2.9. Iso-surface value of the correlation coefficient at 0.05 shown in red and at -0.03 in blue.

(b) Iso-surface of $R_{p'_w(\rho u)'}$ to visualize vortical structure for Mach 7.2. Iso-surface value of the correlation coefficient at 0.05 shown in red and at -0.03 in blue.

Figure 9. Three dimensional distribution of correlation coefficient between wall-pressure and mass flux fluctuations.

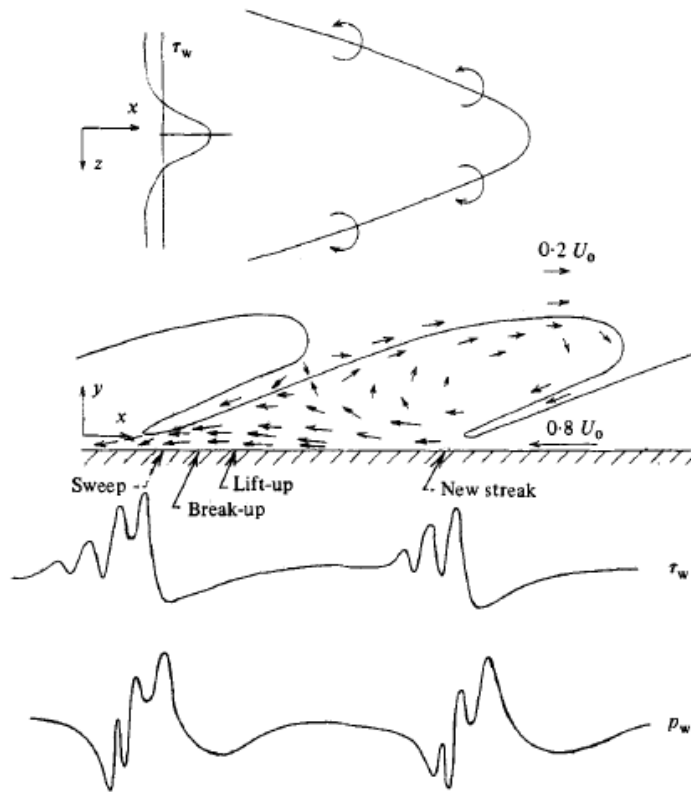


Figure 10. Model of organized structures in turbulent boundary layers from Thomas and Bull,⁴³ after Brown and Thomas,⁴⁰ as seen by an observer moving at $0.8U_0$.

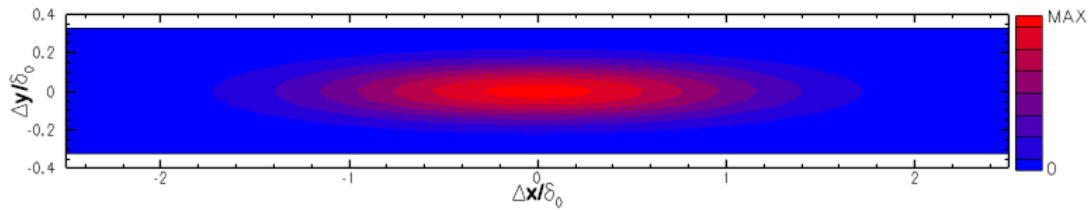


Figure 11. A sample of the finite impulse response filter generated with a bivariate Gaussian distribution to filter out noisy fluctuations which have geometries smaller than a hairpin packet. Figure from Beekman *et al.*³⁴

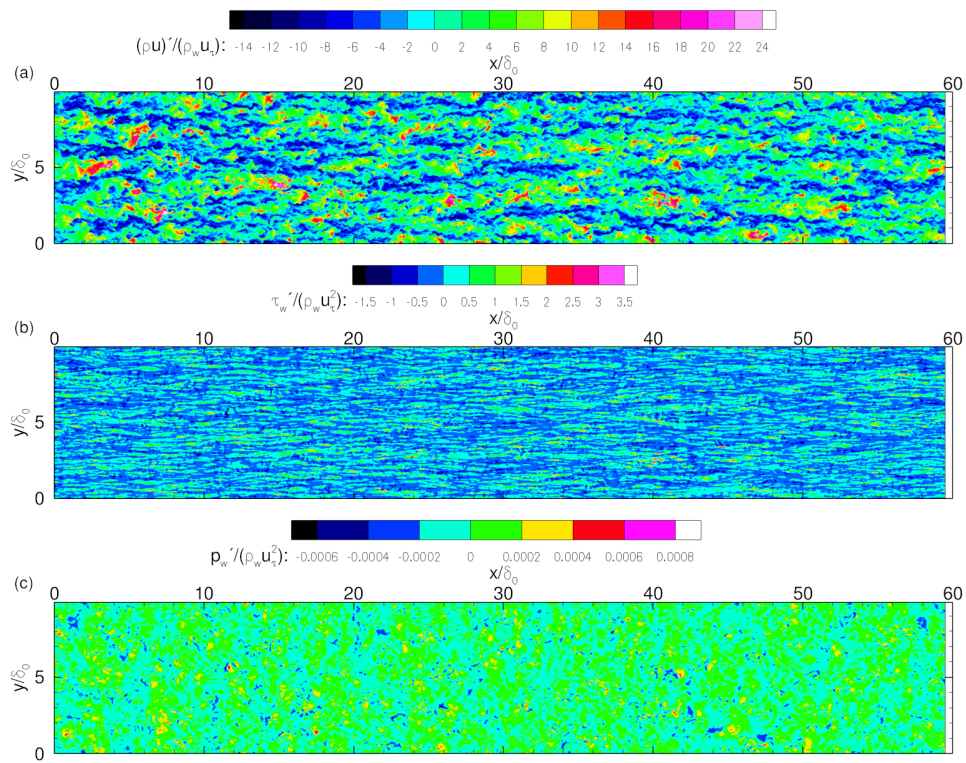


Figure 12. (a) Unfiltered snapshot of normalized streamwise mass flux fluctuations in the logarithmic layer ($z/\delta_0 = 0.2$) for Mach 2.9 case. (b) Unfiltered snapshot of normalized wall-shear stress fluctuations for Mach 2.9 case. (c) Unfiltered snapshot of normalized wall-pressure fluctuations for Mach 2.9 case.

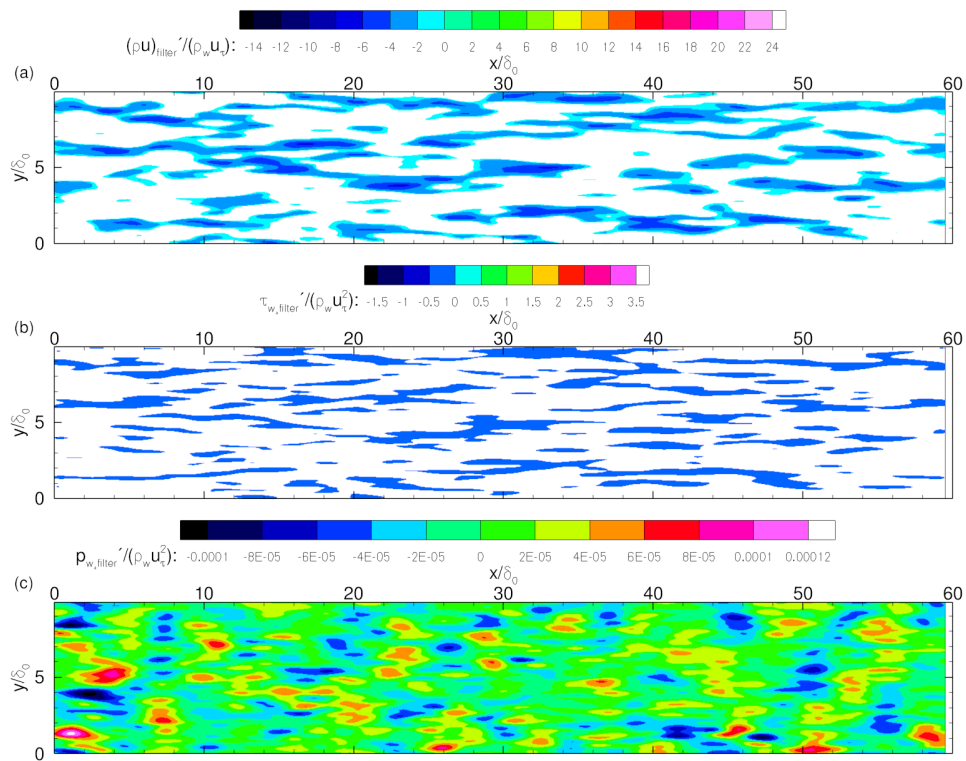


Figure 13. (a) Filtered snapshot of normalized streamwise mass flux fluctuations in the logarithmic layer ($z/\delta_0 = 0.2$) for Mach 2.9 case. (b) Filtered snapshot of normalized wall-shear stress fluctuations for Mach 2.9 case. (c) Filtered snapshot of normalized wall-pressure fluctuations for Mach 2.9 case.

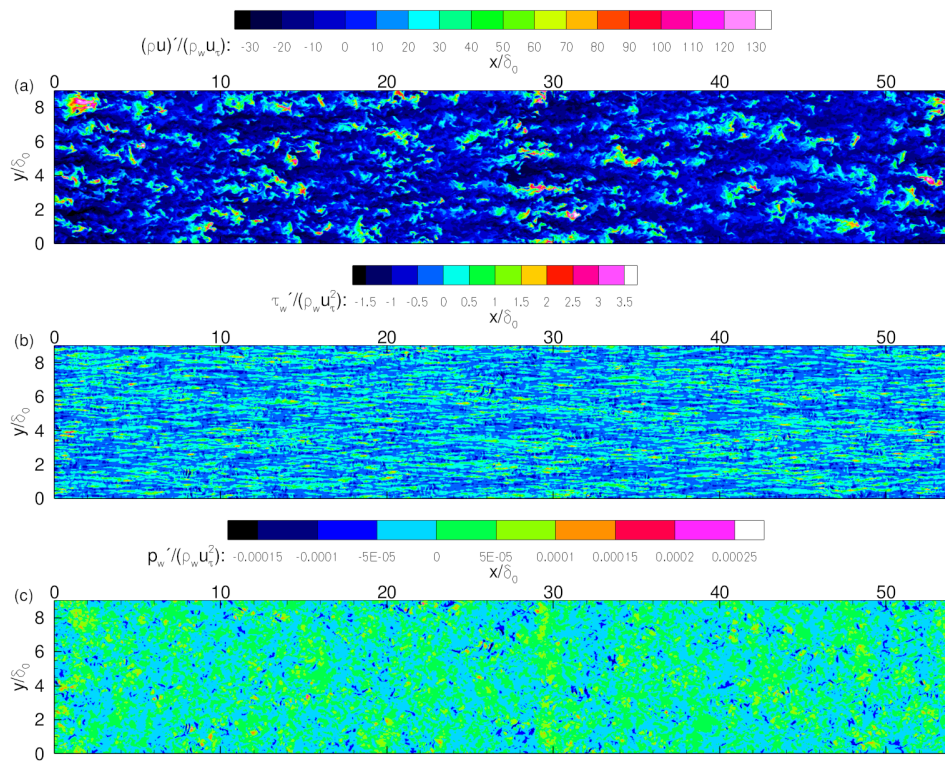


Figure 14. (a) Unfiltered snapshot of normalized streamwise mass flux fluctuations in the logarithmic layer ($z/\delta_0 = 0.2$) for Mach 7.2 case. (b) Unfiltered snapshot of normalized wall-shear stress fluctuations for Mach 7.2 case. (c) Unfiltered snapshot of normalized wall-pressure fluctuations for Mach 7.2 case.

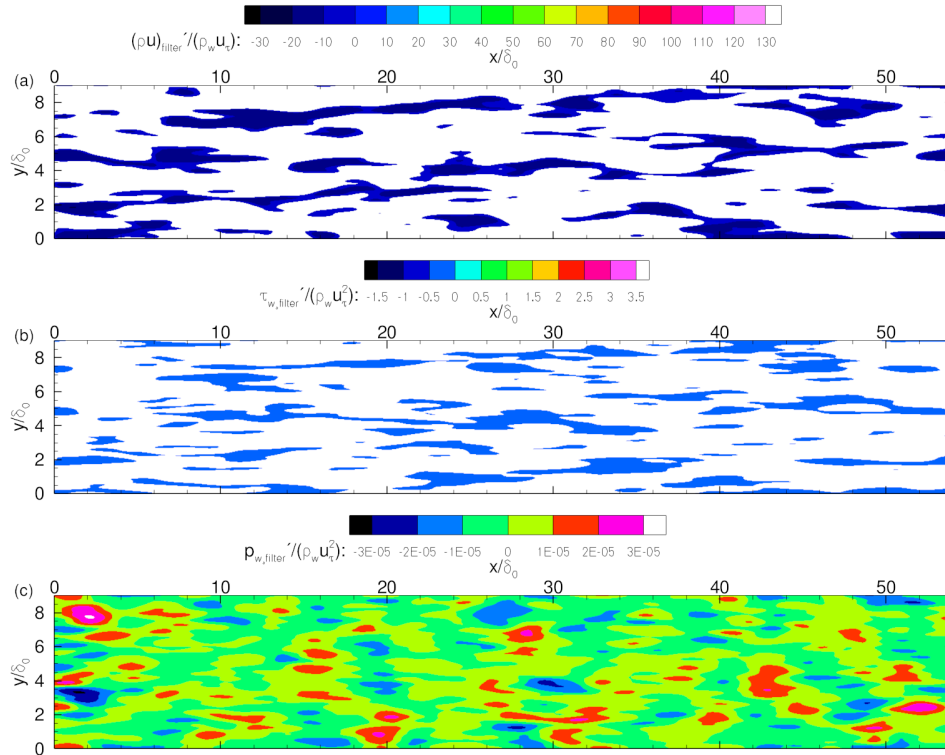


Figure 15. (a) Filtered snapshot of normalized streamwise mass flux fluctuations in the logarithmic layer ($z/\delta_0 = 0.2$) for Mach 7.2 case. (b) Filtered snapshot of normalized wall-shear stress fluctuations for Mach 7.2 case. (c) Filtered snapshot of normalized wall-pressure fluctuations for Mach 7.2 case.

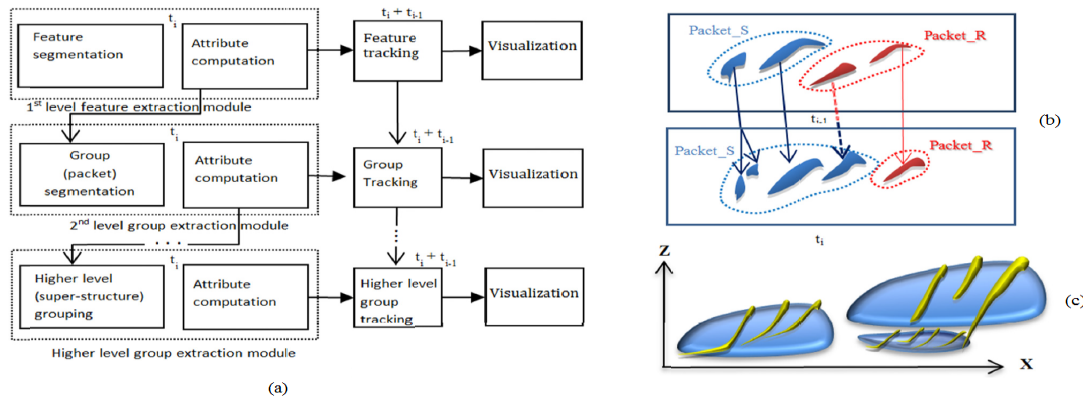


Figure 16. (a) Generalized tracking model that allows the tracking of packets and super-structures of packets of activity tracking algorithm;⁴⁶ (b) An illustration of activity tracking algorithm⁴⁶ where a feature moves from Packet_R to Packet_S. In Packet_S, within the iterative process, unphysical proliferation of packets is prevented; (c) An illustration of packets (formed of yellow hairpins) from activity tracking algorithm.⁴⁶ Three groups of packets are part of a larger packet.

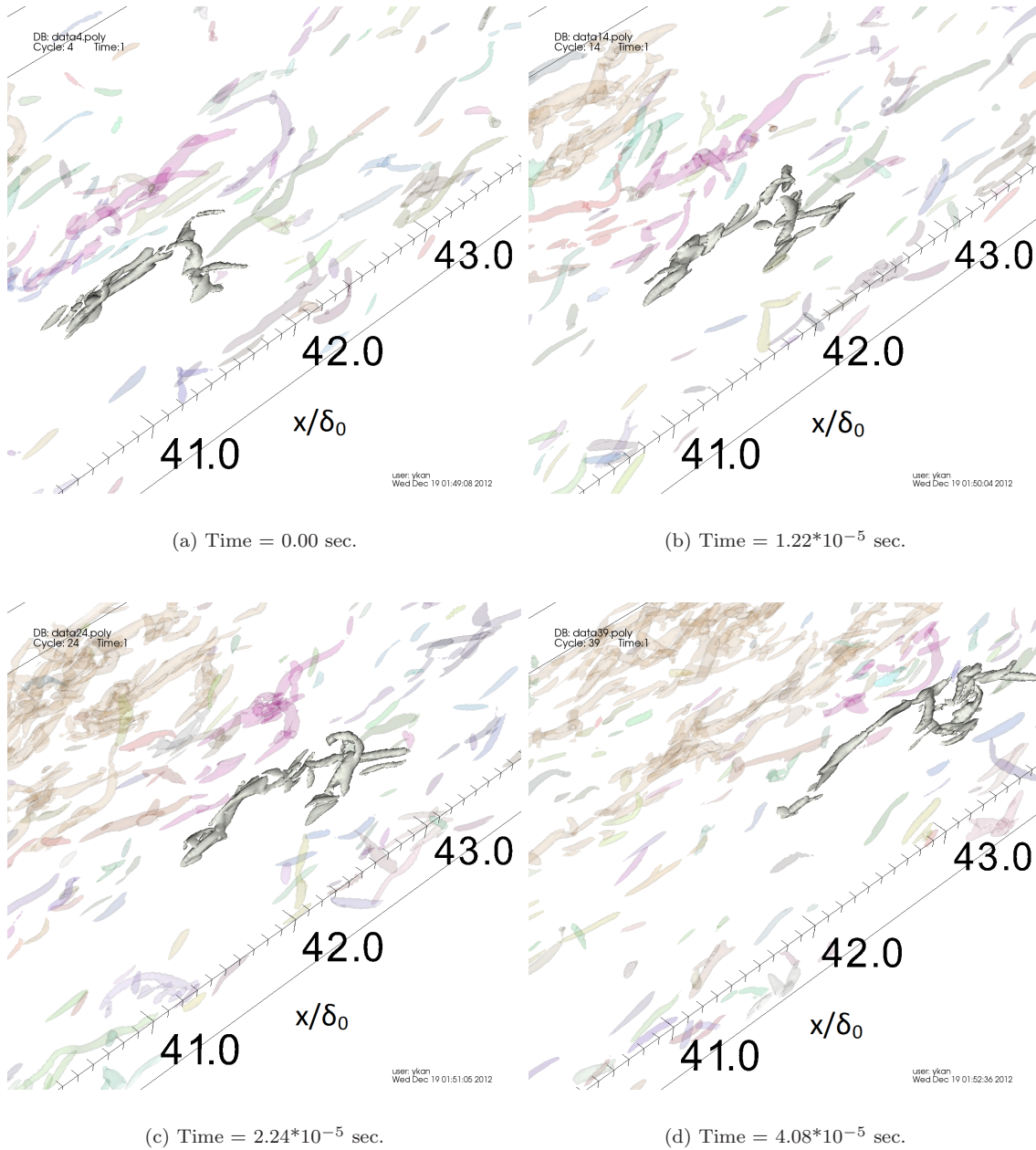
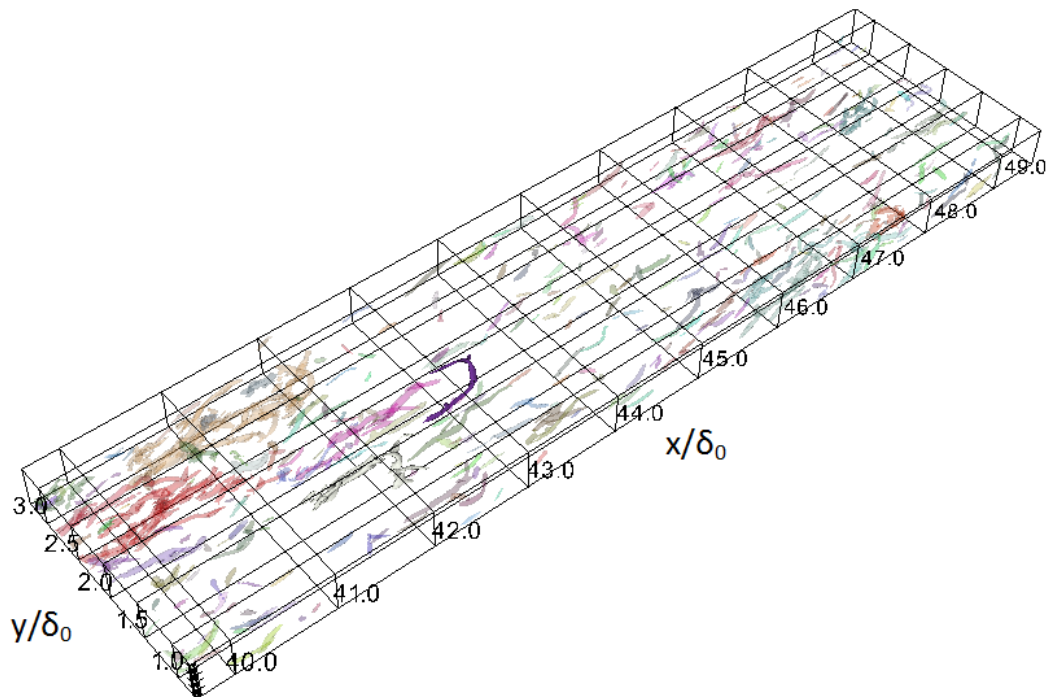
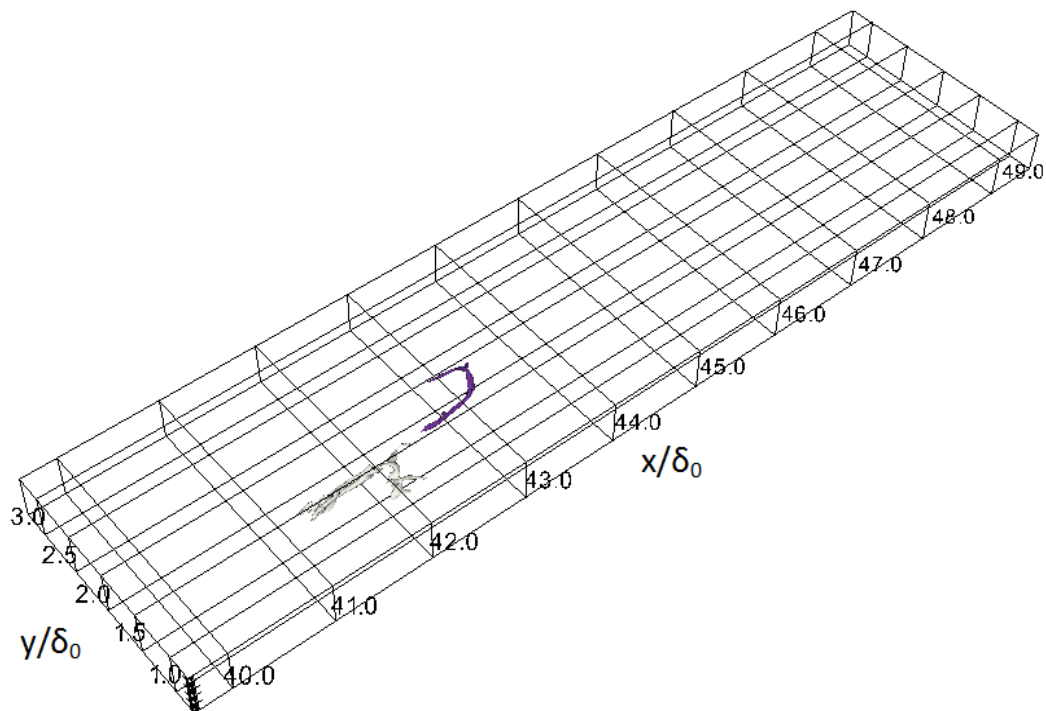


Figure 17. Temporally evolution of a geometrically ‘strong’ packet in the Mach 2.9 dataset in four different time realizations, where sampling rate is $1.20 \cdot 10^{-6}$ sec. Other identified packets are shown at 90% translucency.



(a) Packets that are to be tracked are shown in solid color, where as other identified packets are shown at 90% translucency.



(b) Packets that are to be tracked are shown only.

Figure 18. Two hairpin packets tracked in the DNS data of Mach 2.9 turbulent boundary layer. Structures are visualized by an iso-surface of swirling strength at $4.5\lambda_{ci}^2$. Both packets and their wall signatures are subsequently tracked are identified in Figure 19 and Figure 20.

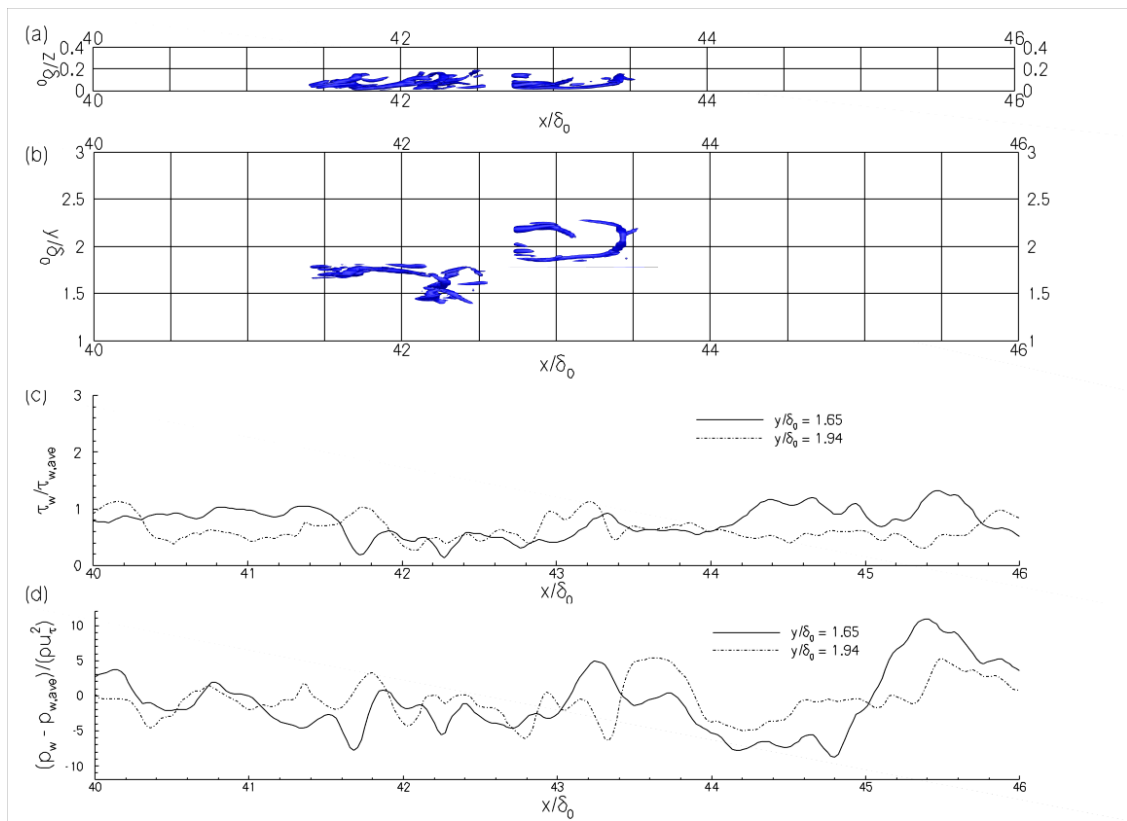


Figure 19. Wall-shear stress and wall-pressure signatures of two geometrically ‘strong’ hairpin packets in the DNS data of Mach 2.9 turbulent boundary layer. (a) and (b) show the streamwise-wall normal plane and streamwise-spanwise plane, respectively, over two packets, visualized by the iso-surface of swirling strength at $\lambda_{ci}^2 = 4.5\overline{\lambda_{ci}^2}$. (c) and (d) plot the wall-shear stress and wall-pressure signals along the mid-span of the hairpin packets.

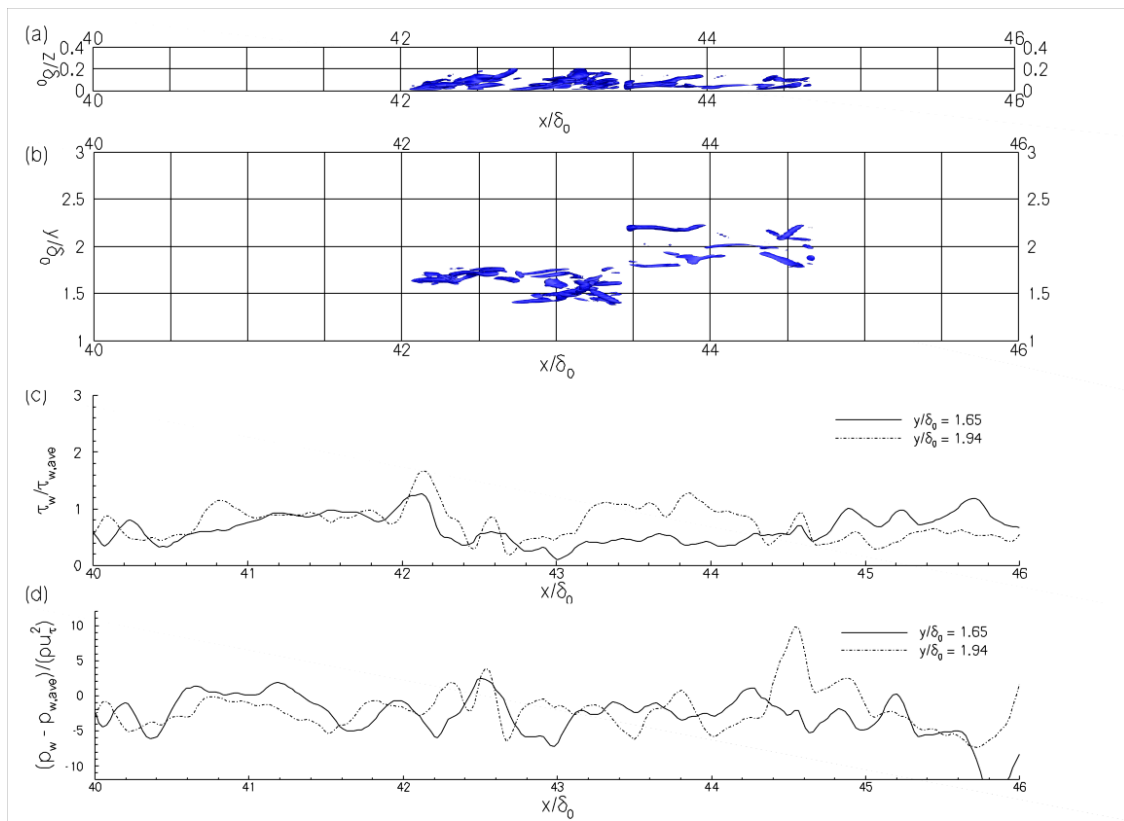
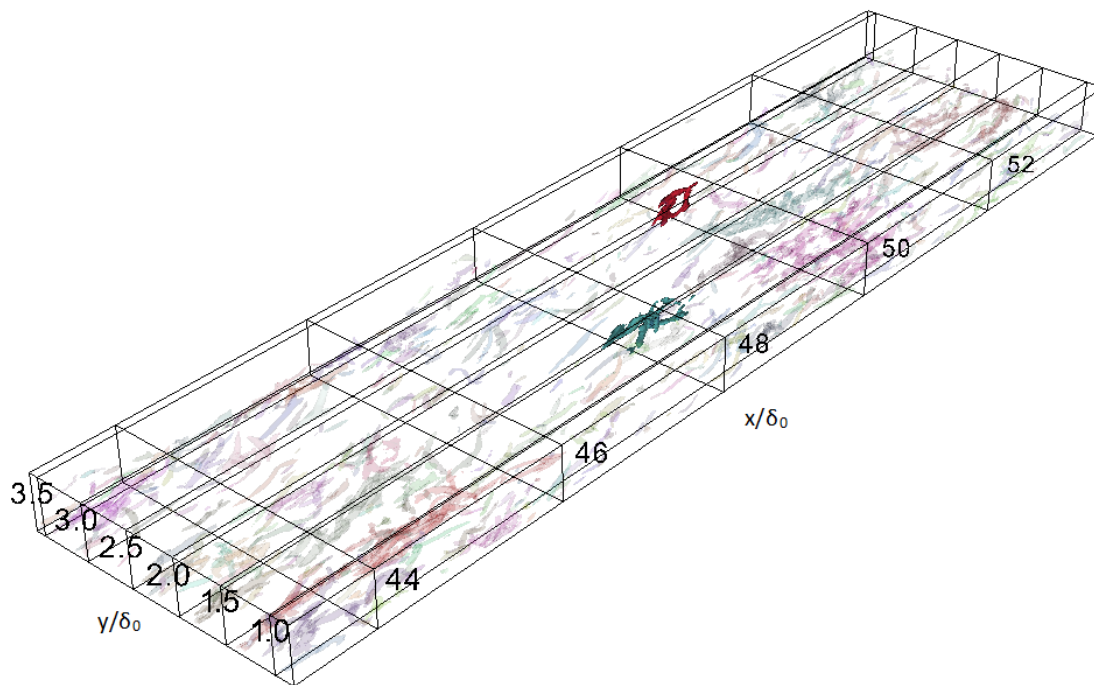
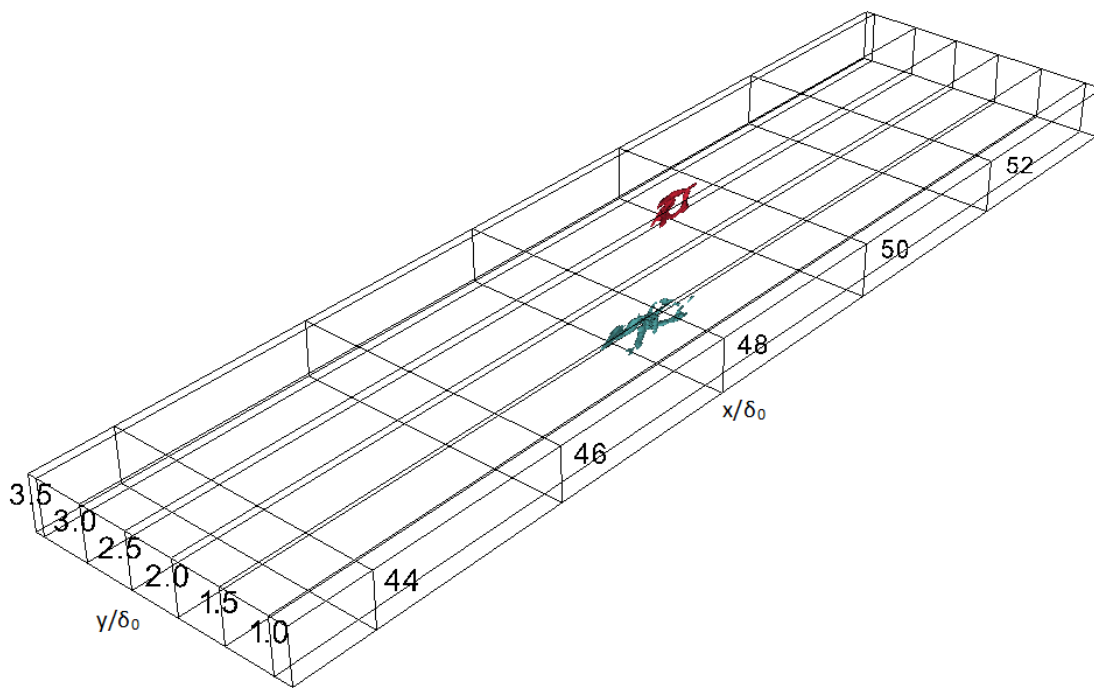


Figure 20. Same plot as Figure 19 but at later timestep where both packets travel a distance of approximately δ_0 .



(a) Packets that are to be tracked are shown in solid color, where as other identified packets are shown at 90% translucency.



(b) Packets that are to be tracked are shown only

Figure 21. Two hairpin packets tracked in the DNS data of Mach 7.2 turbulent boundary layer. Structures are visualized by an iso-surface of swirling strength at $4.5\lambda_{ci}^2$. Both packets and their wall signatures are subsequently tracked are identified in Figure 22 and Figure 23.

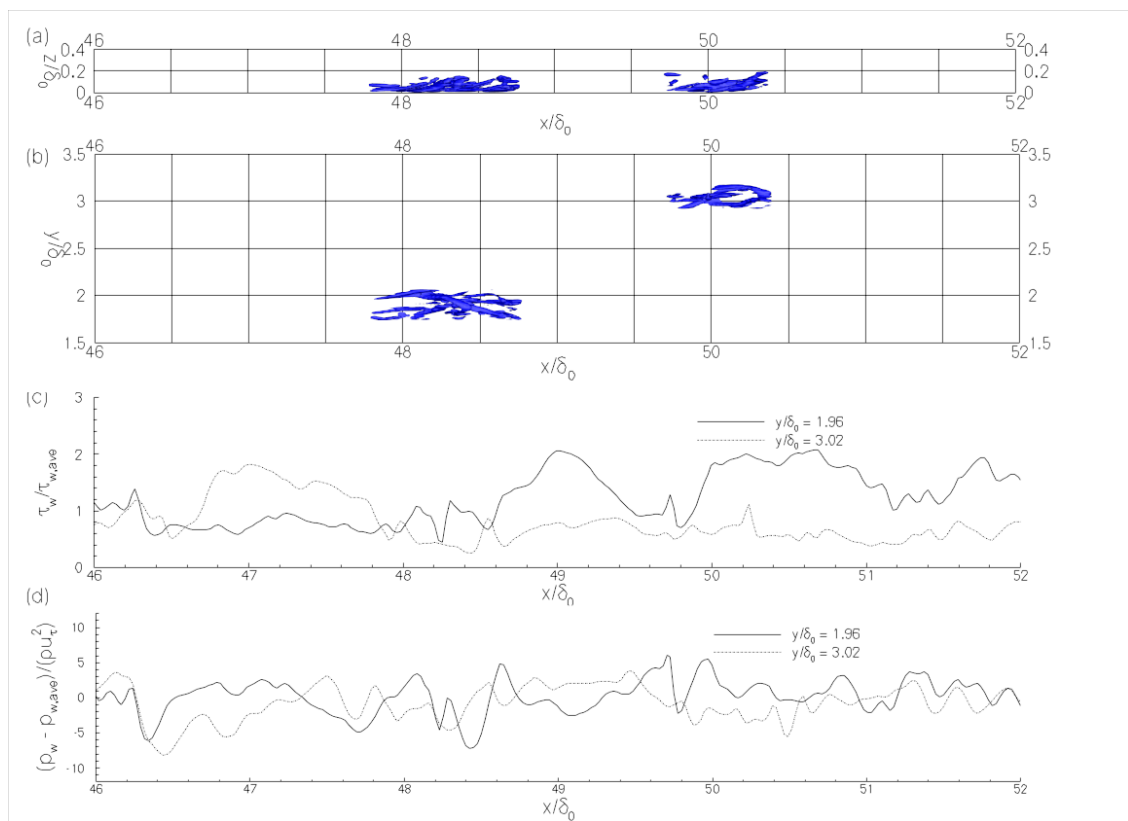


Figure 22. Wall shear stress and wall-pressure signatures of two geometrically ‘strong’ hairpin packets in the DNS data of Mach 7.2 turbulent boundary layer. (a) and (b) show the streamwise-wall normal plane and streamwise-spanwise plane, respectively, over two packets, visualized by the iso-surface of swirling strength at $\lambda_{ci}^2 = 4.5\lambda_{ci}^2$. (c) and (d) plot the wall-shear stress and wall-pressures signals along the mid-span of the hairpin packets.

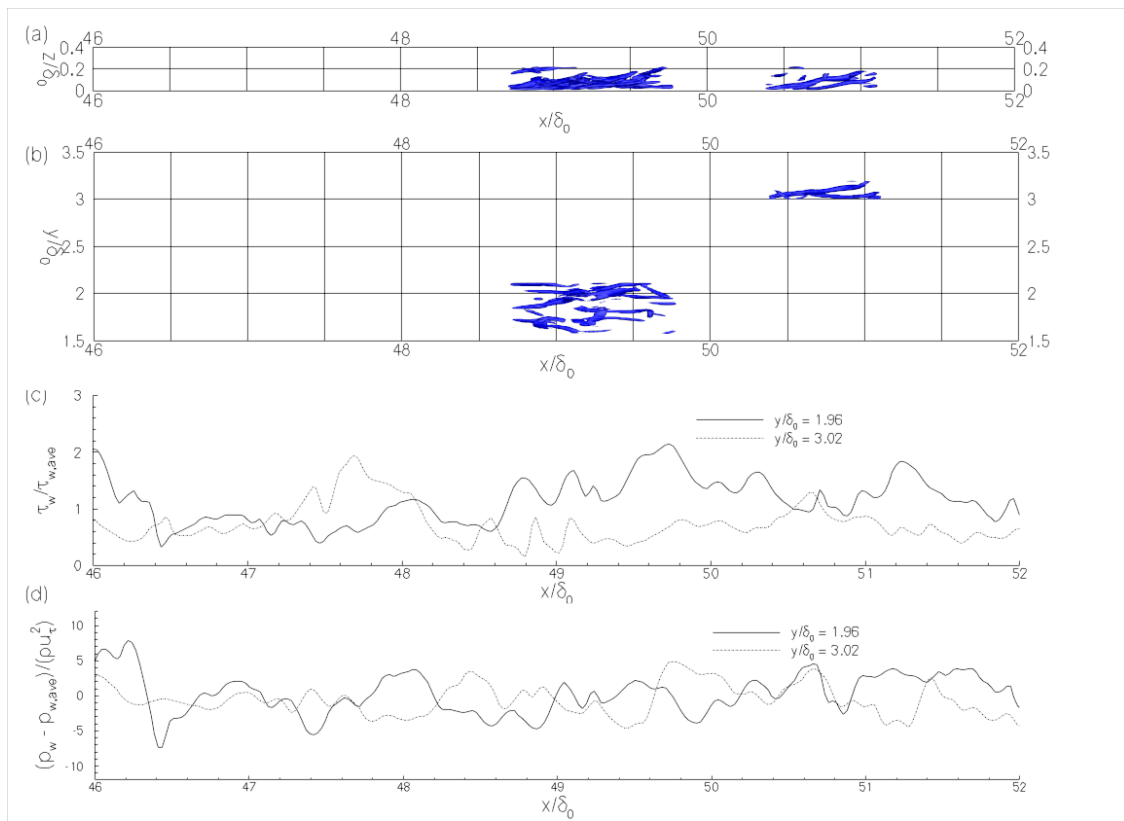


Figure 23. Same plot as Figure 22 but at later timestep where both packets travel a distance of approximately δ_0 .